High-speed scattered-light imaging for sizing respiratory droplets

Roth, Adrian; Frantz, David; Stiti, Mehdi; Berrocal, Edouard

Published in:
Journal of Aerosol Science

DOI:
10.1016/j.jaerosci.2023.106257

2023

Document Version:
Publisher's PDF, also known as Version of record

Journal of Aerosol Science 174 (2023) 106257

Contents lists available at ScienceDirect

Journal of Aerosol Science

journal homepage: www.elsevier.com/locate/jaerosci

High-speed scattered-light imaging for sizing respiratory droplets

Adrian Roth *, David Frantz, Mehdi Stiti, Edouard Berrocal

Department of Physics, Lund University, Sölvegatan 14, 223 62, Lund, Sweden

ARTICLE INFO

Editor: Dr. Chris Hogan

Keywords:
Lorenz–Mie scattering
Respiratory droplets
Particle sizing
High-speed imaging

ABSTRACT

The COVID-19 pandemic has illuminated the lack of knowledge regarding the airborne transmission pathway of disease. The pathway consists of pathogens contained in small particles ejected when speaking and coughing. A crucial characteristic of these particles is their size that is connected to the their suspension longevity in the air as well as the location of generation and deposition within a subject's respiratory system. Sizing of particles launched from the respiratory system is a challenge for a number of reasons: (1) the size of ejected particles varies over a wide range, between sub- to several hundreds of microns, (2) particles are ejected at various speeds in different directions, (3) each single event is unique where for example the number of particles can vary greatly between two occurrences of the same event and subject, (4) the size of the particles vary significantly as they evaporate over time. To overcome these challenges and categorize full coughing and speaking events, new measuring methods are needed. In this work, we present, in detail, high-speed scattered light imaging to size liquid particles (droplets) in unique respiratory events. A high-speed camera records scattered laser light at 16 000 frames per second in a semi-forward scattering direction. The illumination is close to the ejection source which means that the particles are sized before evaporation. The measurement can size stationary droplets from 3.4 to 44 μm and moving droplets from 4 to 80 μm resolved in both time and space. To get a reliable estimation, careful calibration of scattering angles and calibration uncertainty has been performed showing a general uncertainty of 8%. Thus, the approach proposed in this article can provide valuable and accurate data to improve the understanding of the airborne transmission pathway.

1. Introduction

The transmission routes for respiratory diseases such as the common cold, influenza and COVID-19 starts with the ejection of particles from an infected subject's respiratory system when for example speaking or coughing. The particles are then transmitted to another person through either: drop spray transmission where the ejected drops are directly deposited on the eye nose or mouth of another person, aerosol inhalation transmission where the virus-laden particles are small enough to be suspended in the air for a prolonged time before inhalation by another person or surface transmission where the viruses have been deposited on either an animate or in-animate surface that another person comes in contact with Li (2021). The airborne transmission (aerosol inhalation) has been suggested as the main route for the SARS-CoV-2 virus that spreads COVID-19 (Lewis, 2021; Liu et al., 2020; Morawska et al., 2021; Wang et al., 2021), deduced from results that surface transmissions are not as common (Goldman, 2020). Particles ejected from the respiratory system span in size from nanometers to millimeters. A deeper understanding of this size distribution is of great importance since it is connected to transmission in the following ways:

* Corresponding author.
E-mail address: adrian.roth@forbrf.lth.se (A. Roth).

https://doi.org/10.1016/j.jaerosci.2023.106257
Received 5 May 2023; Received in revised form 8 August 2023; Accepted 23 August 2023
Available online 1 September 2023

- Size affect how long particles stay in the air and how far they travel from an infected person. Smaller particles stay in the air longer while larger particles are more likely to deposit on surfaces or reach people at shorter distances (WHO, 2014). A general size limit of 5 μm is found in the WHO regulation (WHO, 2014) where particles below this size are classified as being aerosols that can cause airborne transmission. Recent studies suggest that this limit should be reconsidered to take into account how larger droplets through both clustering and evaporation can have an extended suspension lifetime (Bourouiba, 2020; Wang et al., 2021).
- Particles of different sizes originate from different depths in the respiratory system (Bagheri et al., 2023; Johnson et al., 2011; Wang et al., 2021). At these depths, there may be different pathogen concentrations that affect the spreading. In addition, larger particles from each depth will contain more pathogens proportional to the particle volume that substantially increase with size.
- Particles with different size will be deposited at different depths in the respiratory system of a healthy person that can affect the infection severity (Gralton et al., 2011; Wang et al., 2021).

Too small droplets are not relevant when studying disease transmission. There is a lower particle size limit corresponding to that of the pathogen size. Sizes below that should not be considered since they will not contain any pathogens. For SARS-COV-2 this size corresponds to around one hundred nanometers (Bar-On et al., 2020). Moreover, the concentration of pathogens in particles with different size is as mentioned connected to the respiratory depth where the particles were generated. Bagheri et al. (2023) found that particle sizes > 15 μm mainly originates from the oral cavity, 5–15 μm from the larynx/pharynx and <5 μm from the lower respiratory tract. The type of respiratory disease and production mechanism of the particles might affect this generation. If two particles are generated in such a way that they have the same pathogen concentration, then a particle with a diameter of 5 μm has statistically 27 times fewer number of pathogens compared to a 15 μm particle. The knowledge of particle size distribution is then relevant. If there are 27 times more particles of 5 μm size compared to 15 μm, the infection risk of the smaller particles might be greater since they will stay in the air longer and probe further down in the respiratory system when inhaled. Therefore, it is of great interest to estimate the ejected particle size distribution to further understand which particles carry the largest risk of transmitting disease and in continuation what measures should be taken to neutralize these particles.

When discussing sizes of particles ejected in respiratory events, the role of evaporation should be recognized. Evaporation will largely affect the particle sizes over time after ejection. Even at a relative humidity of 80%, it has been found that particles below 20 μm will shrink to around 5 μm residue particle within seconds (Stiti et al., 2022). Then, the number of pathogens that the particles contain is relative to the volume before evaporation and the residue particle will stay longer in the air and penetrate further into the respiratory system when inhaled. A measurement of sizes close to the mouth should end up with a larger size distribution of "wet" particles compared to a measurement further away of "dry" particles.

In the literature, estimations of the size distributions of respiratory particles have been performed for different kind of events such as breathing, speaking, yelling, singing, coughing, and sneezing using a variety of techniques. The review by Gralton et al. (2011) details sizing measurements up to 2011 and the following is a summary of what techniques have been used.

The earliest approach for sizing wet particles was made in 1946, consisting in using glass plates placed in the path of the person (Duguid, 1946). The droplets that deposited on the plate were then individually sized under a microscope. This is a time-consuming method when it comes to gathering statistically sufficient data. In more recent works three different kinds of instruments have been commonly used, Aerodynamical Particle Sizer (APS) (Alsved et al., 2020; Asadi et al., 2019; Johnson et al., 2011; Morawska et al., 2009; Yang et al., 2007), the Optical Particle Sizer (OPS) (also known as Optical Particle Counter (OPC)) (Bagheri et al., 2023; Lee et al., 2019; Papineni & Rosenthal, 1997; Xie et al., 2009) and the Scanning Mobility Particle Sizer (SMPS) (Bagheri et al., 2023; Lee et al., 2019; Yang et al., 2007). The APS works through a time-of-flight measurement at a certain distance from a change of air-flow speed. The particles will accelerate differently depending on their aerodynamical size. The measured time is then used to estimate the size. The APS model 3321, TSI Inc. measures sizes in the range 0.5–20 μm. The OPS and OPC instead works by detection of scattered light from a laser beam. Larger particles scatter a larger intensity which is the principle behind the technique. The OPS Model 3330, TSI Inc. can size particles between 0.3 and 10 μm. The SMPS has a similar detection system as the OPS with the difference that there is a prior liquid condensation onto the particles. Then particle sizes between 0.01 and 0.42 μm are measured for model 3910, TSI Inc. Note that for all these three measurement devices, evaporation plays a role in the measured sizes since there is a significant time from the ejection of particles to detection (Morawska et al., 2009). Some work also makes sure that the measurement is of the dry distribution by adding diffusion driers prior to the sizing (Bagheri et al., 2023).

The APS, OPS and SMPS can measure very small particle sizes. However, the techniques do not fully resolve respiratory events spatially nor temporally. The typical required sample time is between 5 and 60 s to accumulate enough particles for the measurement and it is common to ask subjects to repeat a respiratory event during this time. The ejection phase of a single cough event lasts only a few hundred microseconds. This means that the temporal variations of a single event cannot be resolved with this sampling method. Additionally, there is no information of where particles are produced spatially from a single measurement with these devices. To retrieve such information, a complementary imaging technique can be applied.

Three imaging techniques for sizing have been applied. First is shadowgraphy (de Silva et al., 2021) where the particles are imaged in front of a background illumination and are then sized from the imaged size on the pixel image. In the field of sprays, the technique enables the visualization of droplets in motion down to sizes of around 5 μm using a long-distance microscope (Sjoeberg et al., 1996). While this technique offers exceptional spatial resolution, it comes with a trade-off of a limited viewable area, usually spanning just a few square millimeters. While monodispersed droplet generators can easily facilitate such measurements, applying this approach to human speech becomes challenging due to the unpredictable and transient nature of droplet generation, occurring

both in space and time. Second, is Interferometric Laser Imaging for Droplet Sizing (ILIDS) (Ragucci et al., 1990; Russell et al., 2020) used by Chao et al. (2009). Here, the transparent particles are illuminated by a laser sheet and imaged slightly out of focus. Then, an interference fringe pattern will be found in the images where the frequency of the fringes is related to the particle diameter. Third is Digital Inline Holography (DIH) (Katz & Sheng, 2010) where a diffraction pattern of a laser that has interacted with the particles is imaged (Bagheri et al., 2023; Shao et al., 2021). From the diffraction pattern, the 3D shape of the particle can be extracted which includes its size. All of these imaging techniques suffer from the trade-off between the smallest particles that can be sized and how much of the respiratory event is captured since the particle must be spatially resolved in the images. To be able to size smaller respiratory droplets, one can either zoom to enable higher pixel resolution that will restrict the field of view or increase camera pixel count that will restrict the recording frame rate where typically kHz is required to resolve a respiratory event.

Various light scattering-based methods are employed to detect and visualize exhaled particles, with white light illumination using powerful LEDs being a common approach to image saliva droplets, along with different source/detector configurations. Experiments using back-scattering detection have revealed that large droplets produced from a sneeze can travel distances of over 6 meters (Bourouiba et al., 2014). Side-scattering detection have been utilized to study facemasks and determine their blocking efficiency (Bahl et al., 2021). Semi forward scattering detection schemes have been applied to analyze singing events (Alsved et al., 2020). However, despite their advantages, powerful white light sources are not sufficiently bright for observing the small and fast-moving particles near the mouth. To address this limitation, an intense laser sheet is used to detect micrometric aerosols over a 2D area. This ground-breaking approach was first demonstrated in 1979, where a TV camera served as the detector to image aerosols with diameters less than 1 μm (Webber et al., 1979). This pioneering work paved the way for nearly four decades of Particle Image Velocimetry (PIV) measurements (Adrian, 1984). Today, modern camera phones can also detect light scattered by saliva droplets illuminated with a laser sheet (Anfinrud et al., 2020). The number of droplets detected and the sensitivity of the measurement technique depend greatly on the cameras and lasers used to visualize the droplets.

In this work, we present in detail a temporally and spatially resolved sizing approach that can overcome some of the mentioned limitations of the previously applied sizing techniques. The sizing approach can be applied to any respiratory event. The ejected droplets are illuminated by a high-power laser at a short distance from the mouth. At this distance, evaporation has not yet significantly affected the particle size and water content (Stiti et al., 2022). The scattered laser light intensity from the respiratory droplets are then imaged by a high-speed camera. From the imaged intensity, the droplets are sized via a calibration curve. The calibration curve is estimated from a combination of Lorenz–Mie theory and an in-situ calibration. To be able to size smaller droplets, the camera is placed in the semi-forward scattering direction where the scattering intensity is stronger. This sizing technique is similar to the technique presented in Bertens et al. (2021) where it is applied for measurement of droplets in cloud formation and in Misawa and Yonamoto (2021) where the sizing is applied at low speed to industrial particles. The next section presents the sizing approach, followed by our experimental setup. Section 4 details the calculation of the calibration curve used for the sizing where also a detailed prediction uncertainty estimation is found. Then, the sizing is applied on coughs from three different subjects where results are presented. Finally, tuning possibilities are discussed for this sizing approach.

2. Scattered light imaging approach for droplet sizing

Lorenz–Mie theory describes scattering intensity of light from a homogeneous spherical particle. The calculation of these intensities uses the approximation of Lorenz–Mie solution to Maxwells equations by van de Hulst (1957). The results depend on the properties of particle size, particle refractive index, the illumination wavelength and the scattering angle. The scattering intensity is here the amplitude of the complex phase function where the absolute value uses the same convention as most authors on the topic of scattering use.

In this work the particle refractive index is assumed to be that of pure water, 1.335 - 0.0i since saliva and mucus consists of ∼99% (Humphrey & Williamson, 2001) and ∼95% (Hamed & Fiegel, 2014) water respectively. Surrounding medium is assumed to have refractive index 1.0 - 0.0i. The program MiePlot (Laven, 2003) is used in this work as the implementation of the Lorenz–Mie theory that is based on the BHMIE code described in Bohren and Hoffman (1983). By connecting the particle size to the simulated scattering intensity an inverse calculation of size from intensity can be performed.

To explain the sizing approach, a simplified experimental setup is shown in Fig. 1(a). A spherical droplet is found inside a laser beam where scattering occurs. A camera is placed to image the scattered light and in order to size the particles, the scattering collection angles of the camera is needed. For comparison, two sets of collection angles are shown, one perpendicular between 86°–94° and one in the semi-forward scattering direction between 48°–56°. Scattering intensity depending on particle size and scattering angle is shown in Fig. 1(b). The colored areas correspond to the collection angles for the example cameras. The light collected by the camera I is found by integrating the intensities in the dark red and bright green areas respectively. This gives one point of integrated intensity for each size plotted as stars in Fig. 1(c). From these points, a parametric curve is fitted on the form,

$$\varnothing = a \cdot I^b, \tag{1}$$

where $\varnothing$ is the diameter of the droplet, I is the integrated intensity and a and b are the parameters to be fitted. The fit is a least squares fit of the log–log transform of Eq. (1). The fit is connected to a Root Mean Square Error ($RMSE$) shown in Fig. 1(c). The $RMSE$ gives information of how well the chosen parametric function fits the points of simulated integrated intensities and diameter. Fig. 1(c) show that the semi-forward collection angles both enables detection of smaller droplets (because of higher scattering intensity) and have a smaller error since there is less overlap of intensities for different sizes. Further comparisons of collection angles and tuning of the setup can be seen in Section 6. With the parametric curve in the semi-forward direction, the size of a droplet can be estimated with an imaged intensity. However, the imaged intensity needs to be further calibrated as is discussed in Section 4.

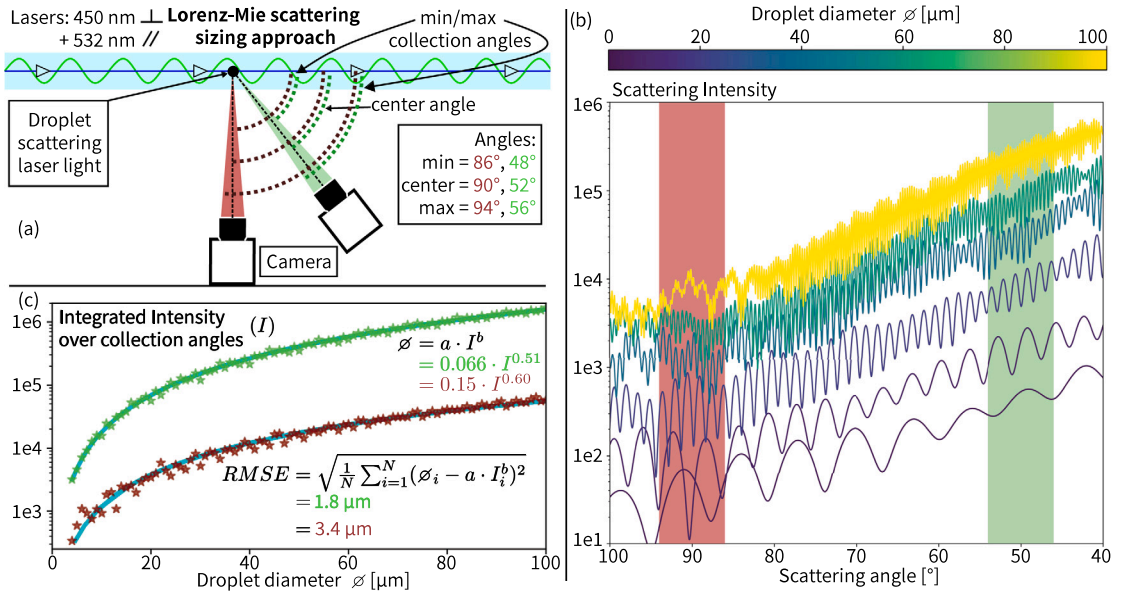

Fig. 1. Approach to size droplets by imaging scattered laser light with comparison between perpendicular (dark red) and semi-forward (bright green) collection angles. (a) A setup where a droplet is found inside a laser beam consisting of two lasers. One laser is at 450 nm with perpendicular polarization and one at 512 nm with parallel polarization. Two center camera collection angles at 90° and 52° are compared. (b) The scattering intensity from droplets with different size as a function of scattering angle simulated using Lorenz–Mie theory. The semi-forward direction has both a higher intensity and less overlap of intensities between different droplet sizes. (c) Stars are the integrated intensity of the darker red and brighter green areas in (b) for all integer sizes between 4 and 100 µm. All stars for each set of collection angles are used to a fit the plotted parametric curves.

3. Experimental setup

The experimental setup is illustrated in Fig. 2 with a view from the top in panel (a) and from the front in panel (b) where also the camera for the sizing calibration is shown. The illumination volume is produced by two continuous wave lasers. One laser is at 450 nm wavelength, perpendicular polarization and 4 W power and the other is 512 nm, parallel and 5 W. The lasers are combined using a dichroic mirror. Then, they are expanded 10 times and truncated by a square aperture with 15 mm side length to a top hat beam with variations of less than 3.5% for the areas where droplets are sized. Finally, the beam is shaped using cylindrical lenses into an illumination volume with of 120 mm height and 15 mm thickness.

A subject is placed behind a protection plate with a quadratic hole of size 15 cm x 15 cm and is wearing protective glasses. The subject is then asked to perform the event that will produce droplets. The droplets will then cross the laser illumination and scatter light into the cameras. The cameras start recording just before the subject starts to produce droplets. Either both Cam. A and Cam. B are recording (calibration phase) or only Cam. A (measurement phase). Both cameras are placed at an approximate center angle of 52° above one another as is seen in Fig. 2(b). The cameras are Phantom VEO 710 high-speed cameras recording with a resolution of 800 × 512 pixels and with 16 000 frames per second. The sensors have 12 bit pixel depth giving a dynamic range from 0 to 4095 counts. Cam. A is imaging the droplet scattering intensity and is equipped with a Nikon objective lens with a collection diameter of 50 mm. With this setup Cam. A has an approximate pixel size of 200 µm/pixel that corresponds to a magnification of around 0.1× (sensor pixel size of 20 µm). All recordings have an exposure time of 50 µs. Cam. B is recording the droplet size for calibration. This camera is equipped with a bi-telecentric (TC16M018 lens from Opto Engineering) lens for 35 mm detectors with 2× magnification where the final pixel size is 10 µm. The telecentric lens has a red band pass filter attached to it that together with a background diffuse red light source form a shadowgraph imaging setup. Cam. B is recording with an exposure time of 6 µs. Example raw images from both cameras are shown in Fig. 2(c). For a discussion on how the choice of experimental parameters such as lasers and detection angle affect the sizing performance, see Section 6.

3.1. Too thin laser thickness, not suitable

In previous work, detection measurements of respiratory droplets using a thin laser thickness of a few millimeters has been applied (Anfinrud et al., 2020; Fischer et al., 2020). This comes with the advantages of higher illumination fluence that make it possible to detect smaller droplets. However, problems can arise with this setup when it comes to *sizing* droplets as is shown in Fig. 3. Two different droplets have been detected with the thin laser thickness of 1.5 mm. One droplet is more than double the size of the other but they still have approximately the same scattering intensity. With a doubling in size, the intensity should approximately be 4 times larger (50000 instead of the measured 12500 counts) to follow the Lorenz–Mie theory. The reason for this significant loss of intensity is that the larger droplet (b) is not fully illuminated in the frame with maximum intensity.

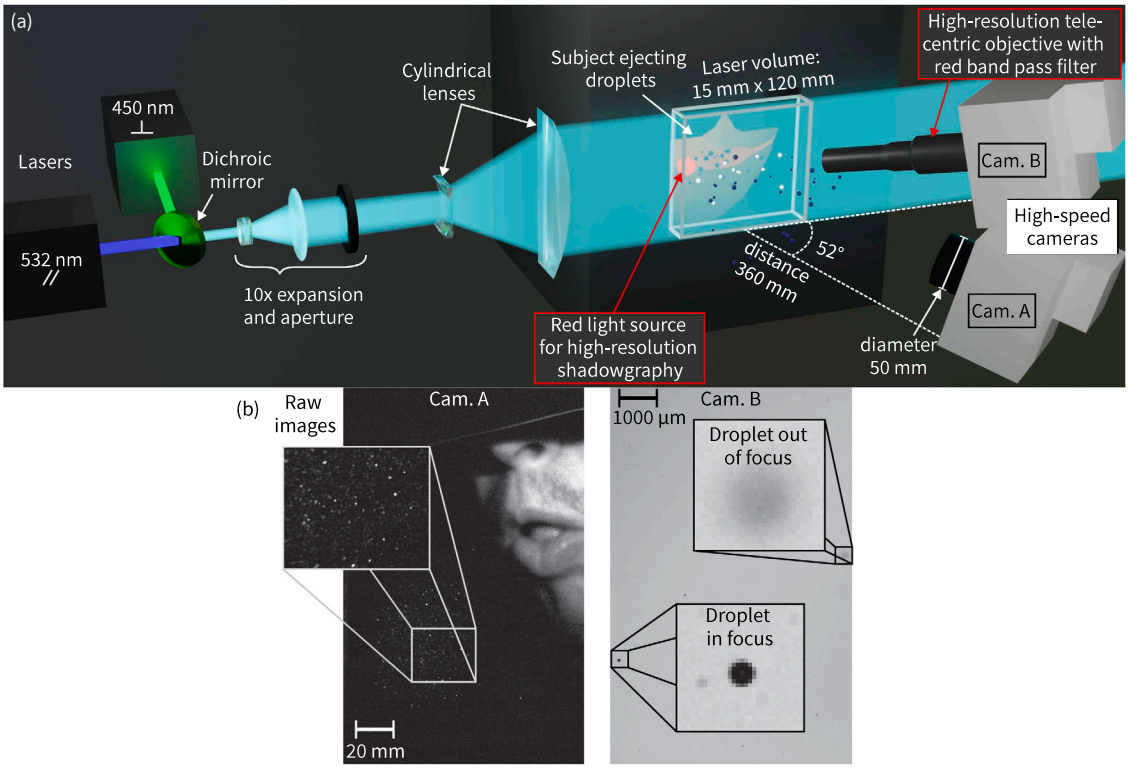

Fig. 2. Experimental setup for sizing droplets. (a) Illustration of the lasers, optics, the high-speed cameras and the subject ejecting droplets. High-speed Cam A. records the scattered light and Cam. B records high-resolution shadowgraph images that can size droplets for calibration purpose. (b) Raw images from Cam. A and B.

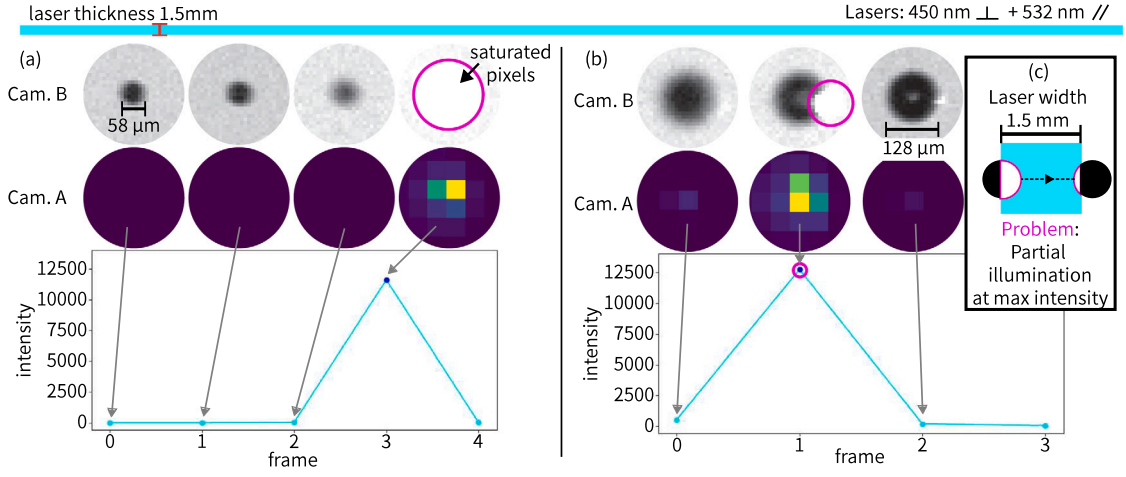

Fig. 3. Size and scattering intensity of droplets showing how a thin laser thickness (1.5 mm) is not suitable for droplet sizing. (a) and (b) show two different detected droplets where the scattering intensity is found with Cam. A and the size is found with Cam. B. Even though droplet (b) is more than double the size of droplet (a), they have almost the same intensity. The reason for this is that droplet (b) is not fully illuminated in the frame with maximum intensity. The pixels inside the pink circles are saturated because of large scattering intensity from the high fluence in the thin illumination volume.

The problem here arises when the particles to be sized are moving too fast relative to the frame rate of the camera and the thickness of the illumination volume. To avoid this problem, an illumination thickness should be chosen so that the fastest particles take at least 3 frames to move through the illumination volume. This ensures that there is at least one frame where the particle is fully illuminated. With 20 000 frames per second recording speed and the max speed of coughed particles as 30 m/s (Mahjoub Mohammed Merghani et al., 2021) an illumination thickness of at least 4.5 mm is required. In this work at least 6 frames is required

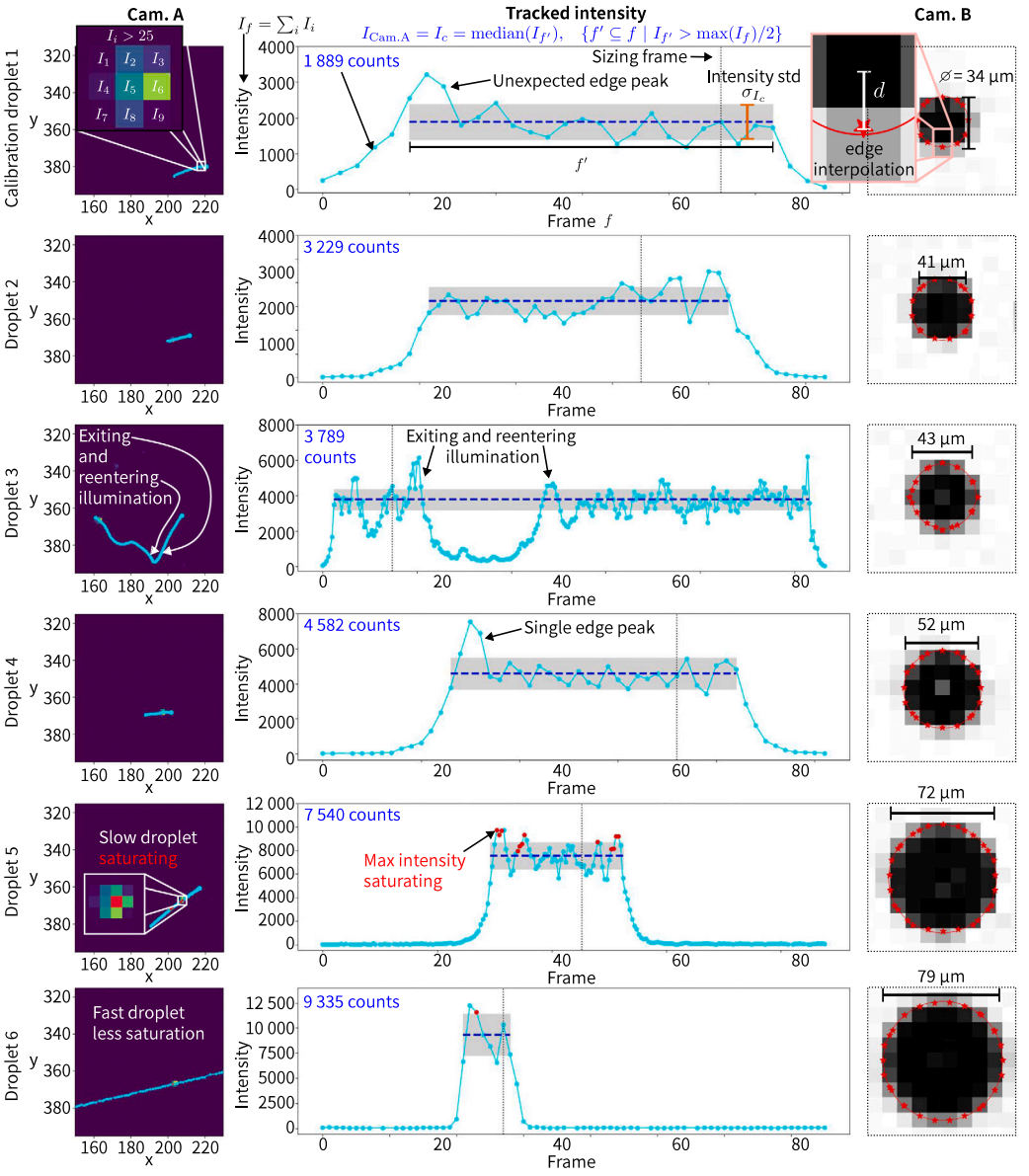

Fig. 4. Tracked intensities and size of 6 example calibration droplets. Left column is the image track for the droplets found in Cam. A. The intensities of the tracked droplet is shown in the center and the right column show the size of the droplet. Calibration droplet 1 illustrate how the intensity at each frame is a sum of pixel counts above a threshold. In addition, a zoom of the edge interpolation distance is shown. This interpolation enhances the size estimation to sub-pixel values.

for the tracking to work which corresponds to a minimum 9 mm thickness. The used 15 mm is then sufficient for the coughed particles that are sized in this work.

4. Sizing calibration

In the calibration phase a person was recorded repeatedly saying the letter "V" to produce a large number of droplets. Known pairs of imaged intensity and diameter of respiratory droplets are extracted with the use of Cam. A to record the scattering intensity I_c and Cam. B to estimate the corresponding droplet size ⌀. Six calibration droplets with correspondences between scattering intensity and size are found in Fig. 4.

Details for how the scattered light intensity and size are extracted are illustrated for calibration droplet 1 in Fig. 4. In Cam. A, the droplet is tracked as is shown by the cyan colored curve. Explanation of tracking is found in Section 4.1. For each frame of this

track the same segmentation as the tracking is used to define an area of pixels using a global intensity threshold of 25 counts. The sum of all pixel values in this area defines the intensity I_f. Note that the imaged light in Camera A is the scattering signature of the particle and not the particle itself since the particle is much smaller than the pixel size. The signal spread over several pixels is due to an effect of the particle movement during an exposure and slight out of focus effects. The intensities of the tracked frames can be seen in the middle column of the Figure. Here, one can see how the droplet has an intensity plateau when fully illuminated. Unexpected edge peaks are also found and is further discussed below. To avoid the edge peaks when calculating the intensity, the subset of the intensities $I_{f'}$ larger than half of the maximum tracked intensity is extracted. The median of this subset is used as the scattering intensity from Cam. A, I_c. The standard deviation of intensities around the median value σ_{I_c} is also calculated to estimate the calibration uncertainty.

The size of the calibration droplets are shown in the right column of Fig. 4. The shown shadowgraphy frame of Cam. B is the one where the droplet was best in focus. To calculate the droplet size from this frame, first a threshold is found as the median value of the background minus the darkest pixel of the foreground droplet. Pixels below this threshold is classified as droplet and the rest as background. To refine the droplet resolution to sub-pixel, an edge interpolation is performed between pixels neighboring the background and the background pixels. The distance d shown for calibration droplet 1 in Fig. 4 is calculated as,

$$d = \frac{\text{threshold} - p_{\text{droplet}}}{p_{\text{background}} - p_{\text{droplet}}}, \tag{2}$$

where p_{droplet} is the pixel value below the threshold and $p_{\text{background}}$ the neighboring background pixel value. d is a value between 0 and 1. It is close to 0 or 1 respectively if the droplet pixel value or the background pixel value is close to the threshold. This sub-pixel refinement is shown as the red stars in the Cam. B column of Fig. 4. These refined edge points are used with a least squares approach to fit a circle where the diameter is the droplet size. By using an 1951 USAF target the minimum size limit for the shadowgraphy was found to be 30 μm, see supplementary data Figure S1. In total, 74 calibration droplets are found above this size.

The intensity curves in Fig. 4 of the calibration droplets have features worth discussing. One observed feature is that almost all intensity tracks of the 90 found calibration droplets have intensity peaks at the left end, right end or even both ends of the intensity plateau. These are indicated for calibration droplets 1, 2 and 4. It has been noted that the peaks are more distinguished for droplets that move slower. This suggests that something is occurring with the scattering if the droplet is imaged close to the edge of the illumination (or even when the droplet is partly illuminated). More calibration data is required to further understand this observation. For calibration point 3, one can see how a droplet is moving irregularly in Cam. A. It is likely that the droplet is then both exiting and reentering the illumination volume. Since this does not significantly affect the scattering intensity it can be concluded that the scattering intensity is unchanged for slightly different positions in the image. Finally for calibration points 5 and 6. Point 5 is saturating the sensor more than point 6 even though it is smaller. The reason for this is most probably that droplet 6 is moving faster than 5. The movement cause a spreading of the scattering intensities over multiple pixels during the exposure which prevents saturation. The maximum limit for sizing a droplet will then depend on the speed of the droplet which is further discussed in Section 4.5. Six additional calibration particles can be found in supplementary data Figure S2.

4.1. Particle tracking

For the calibration and sizing of the droplets (in this subsection denoted particles for generality) must be tracked in Cam. A. The main reason for the tracking is to verify that the droplet is fully illuminated in the frame used for sizing. The tracking algorithm has two parts:

1. Finding of particle pixel position in each recorded frame.
2. Follow particle positions over consecutive frames to create tracks.

1. The following is performed for each image. Pixels that contain background illumination such as of the subjects face is first masked. Then a global threshold of 25 counts is applied. Now a binary image with islands of pixels above the threshold is found. A connected components algorithm is applied to group the islands where each is defined to be a particle. The pixel coordinates of this particle is calculated as the center of mass pixel position weighted by the pixel intensities on the particle island.

2. The tracking used in this work is an in house algorithm that is largely inspired by the Four Frame Best Estimate algorithm (Ouellette et al., 2006) and the extension in Clark et al. (2019). This tracking algorithm is detailed in Roth et al. (2022) and will be explained here in brief. First one position found in the first frame of the previous part is considered. Here, no information of the particle velocity is known. Therefore all possible particle positions in the next frame within a certain max speed from current position is considered in turn. First the closest position is considered. Now a velocity can be estimated from the two positions and it is used to extrapolate where the particle should end up in the next frame. The positions in the next frame within both a distance (max acceleration) of this extrapolated position and within the max speed criteria are considered in turn. Here, the closest position to the extrapolation is first considered. Now both velocity and acceleration of the particle can be estimated from the three positions. The latest position, new velocity and acceleration is then used to extrapolate where the particle should end up in the next frame. All positions within a distance from the extrapolated position (max extrapolation error), within the max acceleration criteria and within the max speed criteria are considered in turn. This process is continued recursively from here on with new positions, velocities and acceleration estimations at each point. A branch in this recursion tree ends when there are no particles found in the next frame within all three distances of max speed, max acceleration and max extrapolation error.

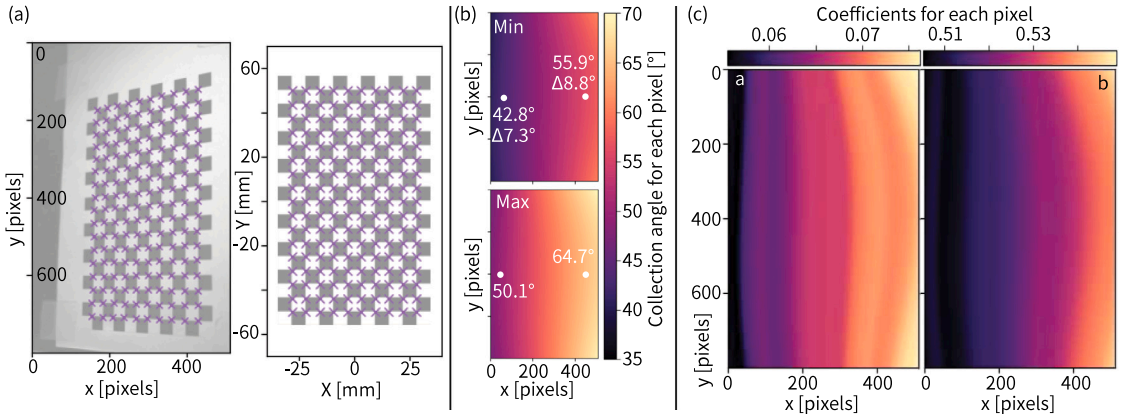

Fig. 5. Camera collection angle calibration. When the droplet is imaged at a specific position in an image, there is a corresponding range of collection angles that should be used. This is taken into account by estimating the parameters a and b in equation Eq. (1) for each pixel. (a) An image of a checkerboard pattern is used and a transform between pixel (left) and world (right) coordinates is found. The transform together with the camera setup parameters is used to estimate the min and max collection angle for each pixel, (b). The collection angles are then used to estimate the coefficients in Eq. (1) for each pixel, (c).

When the full recursion tree has been traversed, the track that is the longest is set to be the best track from this starting position. If there is a tie, the one with smallest sum extrapolation errors is chosen. This is repeated for all found positions in part 1. Then an extraction algorithm is applied to take the best tracks without inducing tracking conflict where two tracks contains the same position. Tracking is repeated for start positions with tracks that induced conflicts followed by extraction. Tracking and extraction is repeated until no conflicts remain. Each track that is 6 frames or longer is considered valid. The maximum speed is set to 20 pixels/frame, maximum acceleration to 2.2 pixels/frame^2 and the maximum extrapolation error to 2.2 pixels. These values have been tuned manually for the coughing events that the sizing is applied to in Section 5. The software used to perform the tracking is open source and can be found at https://gitlab.com/roth.adrian/ptv3py/.

4.2. Camera collection angle calibration

The position of droplets in the illumination volume affect the scattering collection angles of Cam. A. These collection angles will mainly be affected by the pixel position of the droplet in the image since the illumination volume is relatively thin compared to the distance from the camera to the illumination volume. Thus, each pixel have unique collection angles and, in continuation, a specific combination of parameters a and b in Eq. (1). A droplet found in a specific pixel should then be sized using the corresponding parameters of that pixel.

The parameters a and b is estimated for each pixel by using a calibration photo shown in Fig. 5(a). Here, a grid of 19 × 11 checkerboard corners can be seen in both the imaged coordinates (x, y) and the world coordinates (X, Y). The checkerboard is placed in the same plane as the center of the laser illumination volume. With the known corresponding image and world coordinates, a polynomial transform of the third degree is estimated to go from the image coordinates to the world coordinates as,

$$\begin{aligned} X(x,y) &= p_0^X + p_1^X x + p_2^X y + p_3^X x^2 + p_4^X y^2 \\ &\quad + p_5^X xy + p_6^X x^3 + p_7^X y^3 + p_8^X x^2 y + p_9^X xy^2, \\ Y(x,y) &= p_0^Y + p_1^Y x + p_2^Y y + p_3^Y x^2 + p_4^Y y^2 \\ &\quad + p_5^Y xy + p_6^Y x^3 + p_7^Y y^3 + p_8^Y x^2 y + p_9^Y xy^2 \end{aligned} \tag{3}$$

where p_i^d are the coefficients of the transform. Now the world X, Y coordinates for each pixel can be calculated using the transform. With the known camera distance of 360 mm from the origin of the world coordinate system and the lens size of 50 mm, the min and max collection angles can be estimated for each pixel, shown in Fig. 5(b). The collection angle range is varying from around 7° to 9°. Finally, the same procedure that was described in Fig. 1(b) and (c) is used to estimate coefficient a and b for each pixel where the result is shown in Fig. 5(c).

4.3. Extracting final calibration curve

To calculate the final calibration curve, 74 different calibration droplets (six of them are presented in Fig. 4) were found with corresponding intensity and size. This combination of intensity and size is denoted a calibration point. The found calibration points are plotted in Fig. 6(a) where 9 droplets are saturating the sensor in Cam. A and are not used in the following calculations. The criteria for saturation is that at least one pixel in the area of a particle is saturated. The points are used to estimate a scale coefficient $\hat{a}$ by linear least squares,

$$\varnothing = \hat{a} \cdot (a \cdot I_c^b). \tag{4}$$

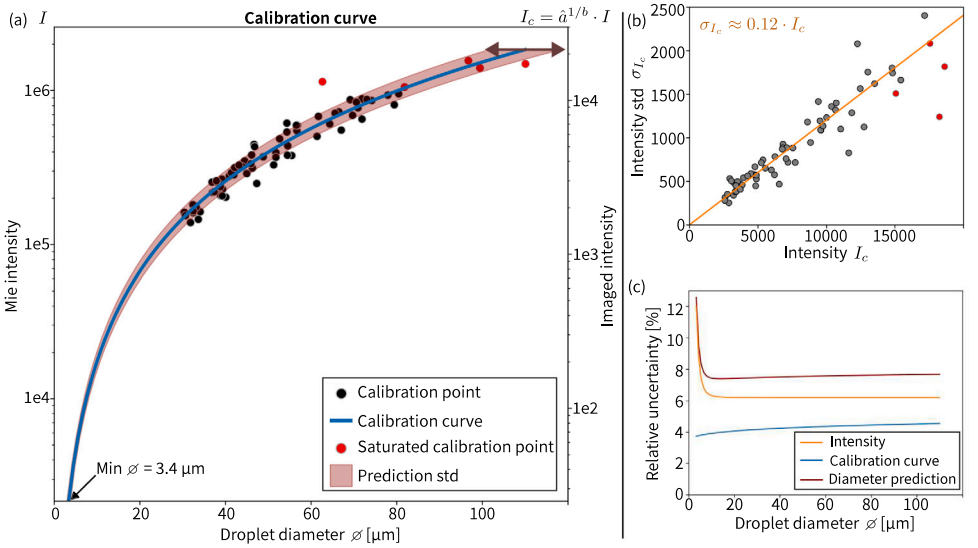

Fig. 6. Calibration curve estimation from calibration points. (a) The black points show single calibration point extracted using the procedure illustrated in Fig. 4. 82 calibration points are used to estimate the final curve. The red area around the curve is the prediction uncertainty. One part of the prediction uncertainty is the uncertainty in imaged intensity. This uncertainty is found to be approximately proportional to the intensity as seen in (b). (c) The relative uncertainty contribution of the intensity and the calibration curve parameters both separately and combined. The corresponding calibration curve for the thin 1.5 mm laser thickness discussed in Section 3.1 can be found in supplementary data Fig. S3.

$\hat{a}$ connects the simulated Lorenz–Mie intensity with the imaged intensity so that the theoretical curves for each pixel can be applied in the experimental setup. Note that the pixel position of the calibration droplets in Cam. A is taken into account in the estimation of $\hat{a}$ by extracting the corresponding a and b from Fig. 5(c). The found scaling ($\hat{a} \approx 9.9$) is then applied to each pixel curve. The shown calibration curve corresponds to the center pixel in the image. With the 25 counts as a minimum image intensity, the calibration curve can size stationary droplets larger than 3.4 µm.

4.4. Size prediction uncertainty

To reliably use this calibration curve, an uncertainty estimation is required. The estimated uncertainty is shown as the red area in Fig. 6(a). This prediction uncertainty consists of two parts. The first part is the uncertainty of the found intensity value which itself consists of two parts.

1. A background noise that is estimated as the RMS value of pixels that image background. This standard deviation is estimated to 5 counts.
2. A standard deviation of the intensity σ_{I_c} was estimated for the calibration droplets (Fig. 4) when the droplet is in the illumination volume. This uncertainty seems to be proportional to the intensity with a proportionality constant of 0.12 as is shown in Fig. 6(b).

Together they give the intensity uncertainty,

$$\sigma_{I_c} = 5 + 0.12 \cdot I_c. \tag{5}$$

The contribution of the intensity uncertainty to the final prediction uncertainty is shown as the orange curve in Fig. 6(c). Generally, the uncertainty is around 6%, however, for droplets smaller than 8 µm the background noise takes over and increase it up to 12%.

The second part of the uncertainty is the uncertainty of the calibration curve. This uncertainty itself consists of the uncertainty of the three parameters in Eq. (4) ($\hat{a}$, a and b). The uncertainty σ_a and σ_b is calculated from the uncertainty in the least squares fit of Eq. (1). The least squares fit was performed after a log–log transform to adapt the equation to linear regression:

$$\log \varnothing = \log a + b \cdot \log I \tag{6}$$

Then, the uncertainty of the estimated least squares parameters is found as,

$$\begin{bmatrix} \sigma_{\log a} \\ \sigma_b \end{bmatrix} = \sqrt{\mathrm{diag}(s^2(\mathbf{D}^T\mathbf{D})^{-1})}, \tag{7}$$

where diag extracts the diagonal of a matrix, s^2 is the estimated variance of the residuals,

$$s^2 = \frac{N \cdot RMSE^2}{N-2}, \tag{8}$$

Table 1
Example values of coefficients and uncertainties. a and b are taken for a pixel in the center of the image.

$\hat{a}$	9.924 ± 0.1 (1%)
a	0.066 ± 0.002 (3%)
b	0.514 ± 0.003 (6%)

where $RMSE$ is the same quantity that is introduced in Fig. 1(c). $\mathbf{D}$ is the regressor matrix of the intercept and log intensity regressor column-stacked,

$$\mathbf{D} = \begin{bmatrix} 1 & \log(I_1) \\ ... & ... \\ 1 & \log(I_{100}) \end{bmatrix}. \tag{9}$$

To extract σ_a, $\sigma_{\log a}$ is propagated through the exponent operator where the value of a also is taken into account. Practically this is performed using the `uncertainties` package in python (Lebigot, 2020). To extract $\sigma_{\hat{a}}$, a similar approach is performed. Then, the $RMSE$ of the fit using Eq. (4) and the 81 calibration points is applied to estimate a second s^2 and a corresponding $\mathbf{D}$ from the regression is,

$$\mathbf{D} = \begin{bmatrix} a_0(I_{c0})^{b_0} \\ ... \\ a_{81}(I_{c81})^{b_{81}} \end{bmatrix}. \tag{10}$$

Note that a specific a and b is used for each calibration point that depends on the pixel position of the found calibration droplet. With the estimated $\sigma_{\hat{a}}$, σ_a and σ_b, the uncertainty of the calibration curve can be calculated. The contribution of the calibration curve uncertainty is shown as the blue curve in Fig. 6(c). Example values of the uncertainties for $\hat{a}$, a and b are shown in Table 1

Finally, the combined uncertainty of both the intensity and calibration curve is propagated to estimate the uncertainty of the predicted size. This corresponds to the mentioned red area in Fig. 6(a) and the relative prediction uncertainty is shown in Fig. 6(c). For small droplets the uncertainty is as large as 13% and otherwise it is generally around 8%.

The OPS instrument has an estimated uncertainty of 5% for a droplet size of 0.5 μm (Han et al., 2011). This was estimated with ISO 21501-1 (in the ISO the uncertainty is denoted resolution). This means that the uncertainty with this technique is higher, however, that is expected since the OPS has a collection angle of 90° ± 60° which should compensate for errors in intensity.

4.5. Measurable size-range depending on droplet speed

The minimum detectable size using the final calibration curve is 3.4 μm. However, this minimum size assumes that all scattered light is collected in a single pixel (Fig. 7(a)) which is possible since the droplet is much smaller than the pixel size of 200 μm. However, if the droplet is moving fast enough, this will no longer be the case (Fig. 7(b)) since the droplet will spread its intensity over multiple pixels during a single exposure. For example, a droplet with size 3.4 μm and a higher speed will no longer be above the detection threshold of 25 counts. A similar case applies for the largest droplet that can be sized. Here, the limiting factor is the saturation of pixels. If the droplet is moving, and therefore spreading its intensity over multiple pixels, a larger droplet can be sized without saturation. To understand the change of sizing range depending on velocity, the effective exposure time must first be described. The effective exposure time is the actual time a droplet is spreading its light into one pixel. The max exposure time corresponds to that of the camera which is 50 μs. A slow droplet will deposit all light into a single pixel and have an effective exposure time of 50 μs. A faster droplet will have a shorter time. This time is connected to a limiting speed where all scattered light is deposited into one pixel v^{lim}.

To estimate the limiting speed v^{lim}, the illustration in Fig. 7(c) is used. Here, a droplet is assumed to be moving in the direction perpendicular to the laser direction at a speed v. Because of the camera orientation at 52° the speed in the camera v_{im} is,

$$v_{im} = \frac{v_c}{\Delta p} = \frac{v\cos(52)}{\Delta p}, \tag{11}$$

where, v_c is the speed projected onto the camera direction and Δp is the size of a single pixel in the camera ($\Delta p \approx 200$ μm/pixel). The distance a droplet travel over a single camera exposure time d_{im} is,

$$d_{im} = v_{im} \cdot \Delta t = \frac{v\cos(52)\Delta t}{\Delta p}, \tag{12}$$

where $\Delta t = 50$ μs. To get v^{lim}, d_{im} is replaced by $d_{im}^{\text{one pixel}}$ that describes the max distance the droplet can travel during one exposure where all scattered light is collected by one pixel. This distance is varying depending on the droplet position inside the pixel and in which direction it is traveling. Through a simple integration of all possible positions and directions, the expected value of this distance is around 0.5 pixels. Therefore $d_{im}^{\text{one pixel}}$ is set to 0.5. By solving for v in Eq. (12) one get,

$$v^{\text{lim}} = \frac{d_{im}^{\text{one pixel}}\Delta p}{\Delta t\cos(52)} = 3.2 \text{ m/s}. \tag{13}$$

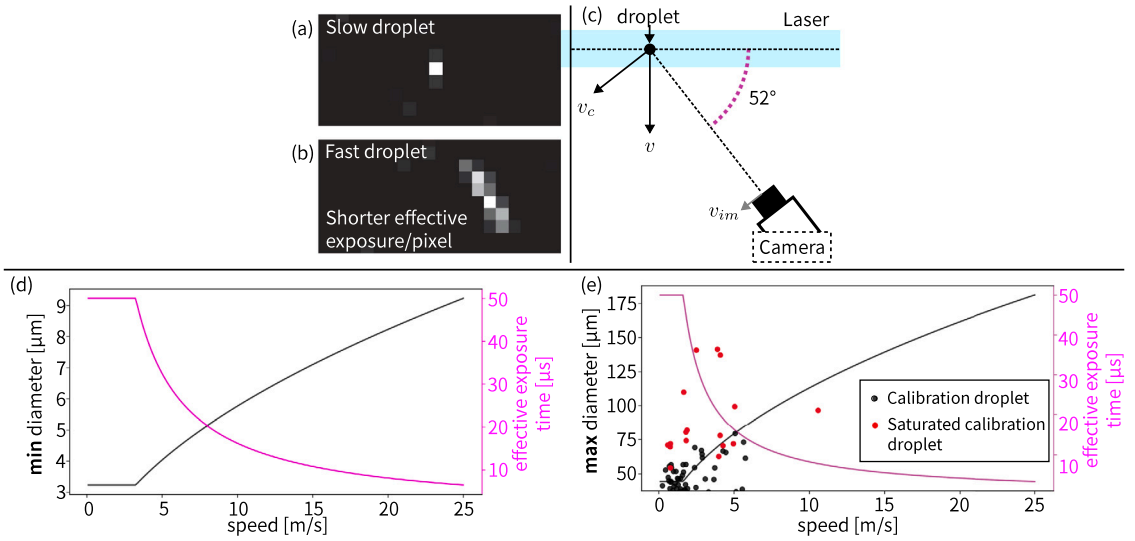

Fig. 7. The size-range of the method depending on the droplet speed. (a) An extracted image from Cam. A showing a slow droplet where all scattered light is collected in a single pixel in contrast to (b) where the droplet is moving fast and the droplet cross multiple pixels during the exposure time. (c) Illustration of how the droplet speed is connected to the speed from the camera perspective. The illustration in (c) is used to estimate the speed dependence of the minimum detectable droplet size $\varnothing_v^{\min}$ (d) and maximum detectable droplet size $\varnothing_v^{\max}$ (e). In each plot the effective exposure time Δt_{eff} of a droplet is also shown. As a comparison between these calculations and the reality, the calibration droplets are plotted in (e). The speed of the calibration droplets is calculated from the tracked v_{im} with the assumed relation Eq. (11).

For speeds below 3.2 m/s the droplet is assumed to have an effective exposure time Δt_{eff} of 50 µs. However, when this speed is exceeded, the exposure time is shortened as,

$$\Delta t_{\text{eff}} = \begin{cases} \Delta t & v \le v^{\text{lim}} \\ \frac{v^{\text{lim}} \Delta t}{v} & v > v^{\text{lim}}. \end{cases} \tag{14}$$

The intensity ratio is then equal to the exposure ratio,

$$\frac{I(\Delta t_{\text{eff}})}{I(\Delta t)} = \frac{\Delta t_{\text{eff}}}{\Delta t} = \begin{cases} 1 & v \le v^{\text{lim}} \\ \frac{v^{\text{lim}}}{v} & v > v^{\text{lim}}. \end{cases}$$

With parameter b of the parametric size curve in Eq. (4) the minimum size as function of speed $\varnothing_v^{\min}$ is,

$$\varnothing_v^{\min} = \begin{cases} \varnothing_0^{\min} & v \le v^{\text{lim}} \\ \left(\frac{v}{v^{\text{lim}}}\right)^b \varnothing_0^{\min} & v > v^{\text{lim}}, \end{cases} \tag{15}$$

where $\varnothing_0^{\min} = 3.4$ µm. The minimum detectable droplet for speeds from 0 to 25 m/s is plotted in Fig. 7(d).

For the largest detectable droplet the limiting factor is the saturation of pixels. This corresponds to 4095 counts which would be sized to around 44 µm. This means that the maximum sizable droplet for a stationary droplet in focus is $\varnothing_0^{\max} = 44$ µm. This size will increase when the droplet is moving with the same reasoning as for the smallest detectable droplet. The main difference is that now the droplet size is almost one fourth of the pixel size. To take this into account the $d_{im}^{\text{one pixel}}$ is halved to 0.25 pixels which corresponds to a $v^{\text{lim}} = 1.6$ m/s. The new v^{lim} and $\varnothing_0^{\max}$ is applied in Eq. (15) to calculate $\varnothing_v^{\max}$ shown in Fig. 7(e). Here, already at a speed of 5 m/s the maximum size is around 80 µm.

The changing size-range are compared to the calibration droplets in Fig. 7(e). From the tracks the average image speed v_{im} is calculated. The relation in Eq. (11) is assumed to extract v for each calibration droplet that is plotted together with its size. There is a possible pattern that faster droplets are less prone to saturate. There is however still the factor of out of focus not taken into account that can explain why there are non saturated droplets above the curve. The saturated droplets below the curve might be connected to how out of focus droplets will not follow the assumed effective exposure relation to speed. This becomes more apparent when the droplet size approaches the pixel size. The sizing limit variation associated with the droplet speed can be removed by using a pulsed laser system. However, a pulsed laser with nano- or pico-seconds long pulses to freeze droplet motion, enough power per pulse to detect small droplets and a repetition rate that matches the high-speed camera is not simple to attain.

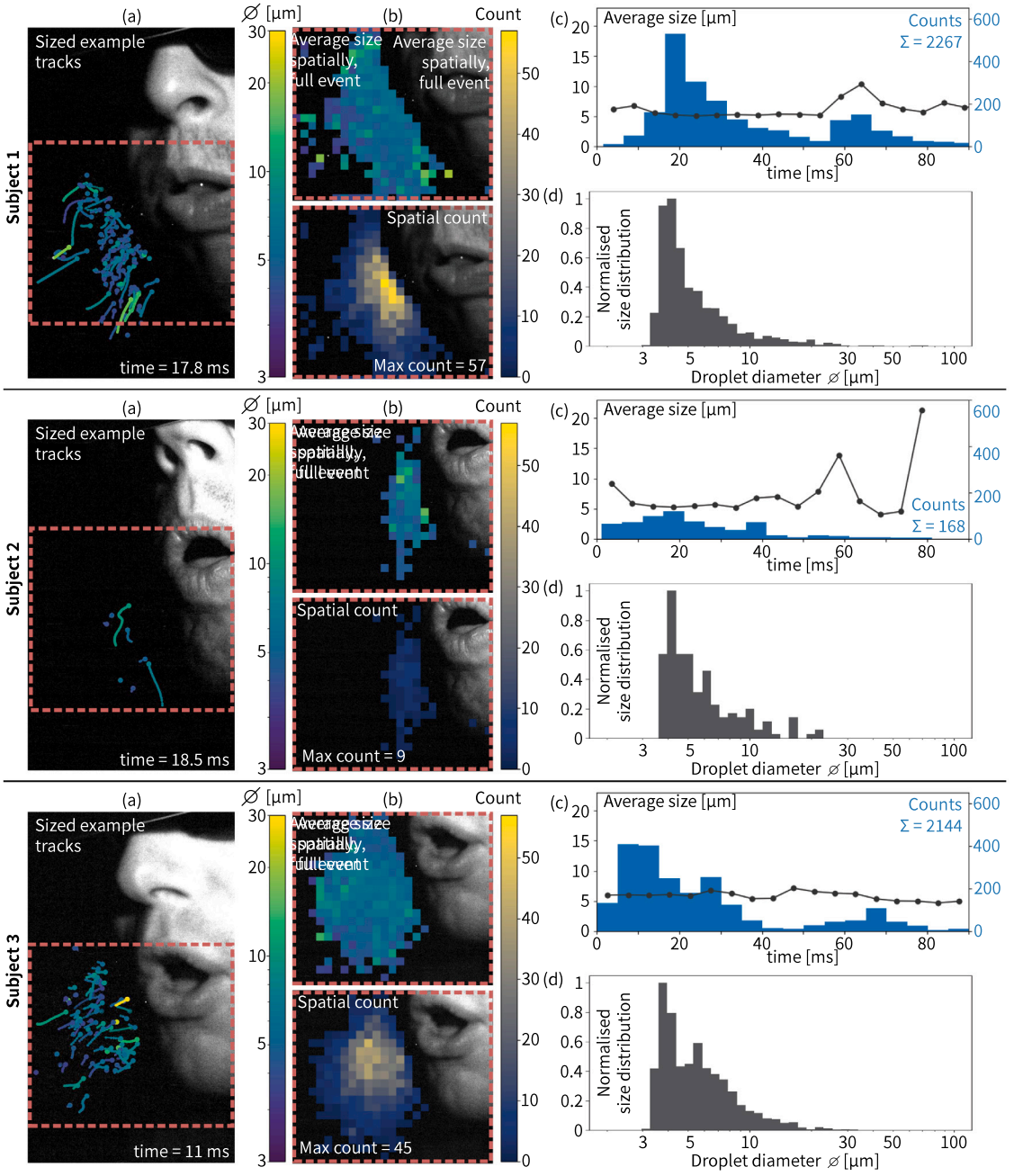

Fig. 8. Sizing results of one cough from three different subjects. (a) The found tracks at one time point and estimated size of the individual droplets according to the colorbar. (b) The average size for droplets depending on the spatial position in the image together with the corresponding spatial count of droplets found at each position. (c) The average size of droplets over time together with the number of sized droplets. (d) The distribution of sized droplets for the full cough.

5. Sizing applied to coughed droplets

Droplets from one cough of three different healthy subjects of male sex have been sized and the results are shown in Fig. 8. Both tracking and extraction of the scattering intensity is performed in the same way as described in Section 4. The calibration curve is then applied to estimate the particle size.

A first conclusion from these results are that subject 1 and 3 have similarity in the production of more droplets compared to subject 2. This large variation in number of droplets for the same kind of event has been previously noted in the literature (Alsved et al., 2020; Asadi et al., 2019; Bagheri et al., 2023; Lindsley et al., 2012).

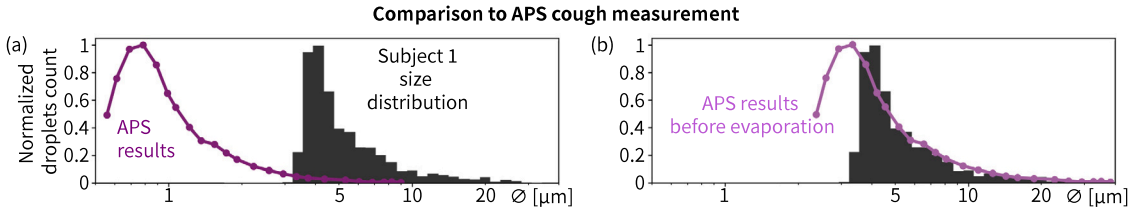

Fig. 9. Comparison between APS and the technique presented in this paper. (a) Raw APS data extracted from Figure 3 in Morawska et al. (2009) together with the size distribution of Subject 1. (b) The APS distribution transformed to sizes before evaporation using the evaporation model presented in Stiti et al. (2022).

Since imaging is used here, there is spatial information of droplet sizes (Fig. 8(b)). From these results, no clear correlation between spatial position and droplet size is visible. Although areas with few droplets (Subject 2 and edges of Subject 1 and 3) inherit a larger variance in the average size which explains why there is an apparent large size for some positions in the image. With fewer droplets at a time point, one single large droplet will have a large effect on the average. The spatial distribution of the droplets show for all subjects how most droplets are found in the center which corresponds to the center of the air jet produced by the cough.

Not only spatial information is found but also temporal from the high-speed recordings (Fig. 8(c)). Similar observations are found here as for the spatial domain. No clear change in size except when there are fewer droplets for a time point. One exception is subject 1 that produce some larger droplets after 60 ms. For both subject 1 and 3 there are two temporal peaks of droplet production. The second peak could be produced by saliva that after a delay reach contact with the streaming air and are ejected. This reasoning is similar to why the number of ejected droplets can vary greatly for the same subject and event (Alsved et al., 2020).

5.1. Counting efficiency

Counting efficiency describes how many of the actual droplets that the sizing technique detects for each size. For the size distributions (Fig. 8(d)), it seems that 4 µm droplets have the highest concentration. Measurements on respiratory events show that the size for highest droplet concentration is significantly smaller than this (Bagheri et al., 2023). This means that a majority of the droplets between 3.4 µm (the definite lower sizing limit of the calibration curve) and 4 are not detected in these measurements. The reason for this is most probably the speed and out of focus effects of the droplets discussed in Section 4.5. The small droplets then generally seem to have a higher speed than 5 m/s. If this speed is also assumed for the larger droplets, the maximum size is then around 80 µm.

The performance of the sizing is largely depending on the performance of the droplet tracking. Examples of such tracks are shown in Fig. 8(a). This is closely linked to the counting efficiency of this sizing technique. The tracking algorithm used in this work is as mentioned built upon the work of Clark et al. (2019) where they estimate their tracking performance by applying their tracking to simulated tracks found in the John Hopkins Turbulence database. The main difference to the tracking algorithm in Clark et al. (2019) is that the tracking algorithm used in this work recursively traverses more possible tracks to find the optimal one. This makes it possible to use their tracking performance results to evaluate the tracking for these three subject. Clark et al. found that their tracking performance largely depended on the so called displacement-spacing ratio. This is the ratio between the average displacement of droplets and the spacing between the droplets. The tracking is harder when there is a larger displacement of the droplets relative to the distance between them. For the data used in this work there is a general displacement spacing ratio below 0.25 with a few peak values of 0.5. This corresponds to a 3% and 10% number of incorrect tracks respectively (Figure 2 in Clark et al. (2019)). In the future, a quantification of the counting efficiency as function of the size is required.

5.2. Comparison to aerodynamical particle sizer results with evaporation correction

The work in Morawska et al. (2009) measured the size distribution of subjects coughing using the APS. Their results (Figure 3 in Morawska et al. (2009)) have been extracted and plotted in Fig. 9(a) together with the size distribution of the cough from Subject 1. A direct comparison is however not possible since the APS measure the evaporated size distribution and the work in this paper measure before evaporation. An evaporation model is used here to correct the distribution, presented in Stiti et al. (2022) that considers saliva as a binary mixture of water and salt using a concentration of salt of 6 g/kg. to transform the APS results to the distribution before evaporation Fig. 9(b). Measurements with the SMPS with evaporation correction show how there is a larger concentration of particles below 3 µm that cannot be detected by either the technique presented in this work nor the APS (Bagheri et al., 2023). The APS is however seen to have a higher counting efficiency below 4 µm droplet sizes.

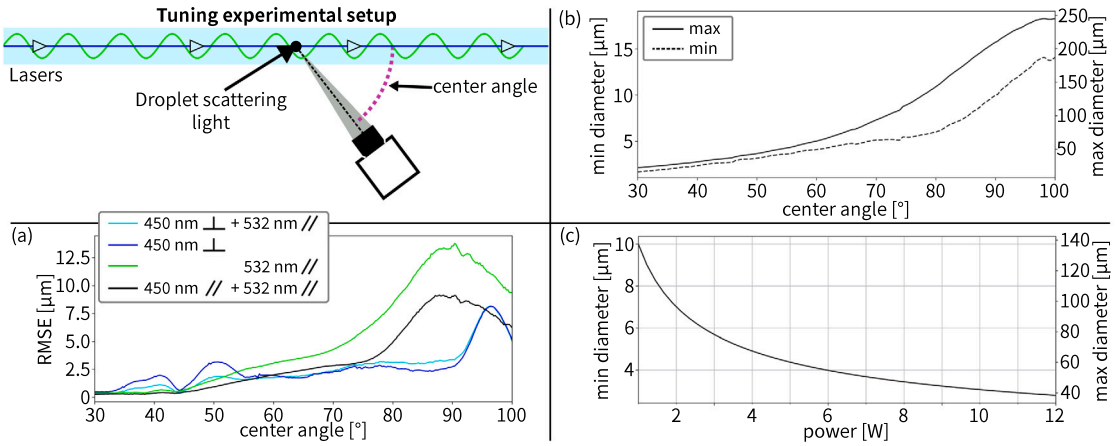

Fig. 10. The three different experimental parameters: laser configuration, center angle and laser power are considered for tuning. (a) Show how the $RMSE$ (introduced in Fig. 1(c)) is affected by different laser configurations and the center angle. (b) Show how the minimum and maximum detectable diameters are affected by the choice of center angle. Finally, (c) show how min and max detectable diameters are affected by the full laser power. Note that when changing one parameter, all other parameters of the experimental setup is assumed to be the same as is used in this work. Therefore the absolute numbers might differ for a different setup but the trend should be the similar.

6. Tuning of the experimental setup

In this section, setup parameters are considered which can help to tune this technique for other measurement requirements, such as different sizing range. The parameters to tune are: the center angle of the camera that defines the main scattering direction, the laser configuration used and the laser power input. Note that the parameters are analyzed mainly by changing one or two and keeping the remaining ones constant. The coupling between the parameters can probably be neglected in most cases which means that a change of multiple parameters at once should follow the sum of the individual changes as detailed below.

Firstly the center angle together with the laser configuration is considered. In this work two lasers were used, one 450 nm with perpendicular polarization and one 532 nm with parallel polarization. The polarization is here parallel or perpendicular to the ground that roughly translates to the camera viewing plane. The two lasers together with a general center angle of 52° gave a $RMSE$ fit value of 1.8 µm that was calculated in Fig. 1(c). The $RMSE$ value is a measure of how well the Lorenz–Mie scattering theory follows the parametric curve Eq. (1), lower value corresponds to an improved fit. In Fig. 10(a) the $RMSE$ value is calculated for different laser configurations and center angles. The current use of two lasers with different polarization is slightly better compared to using a single laser. But the optimal combination is to use both lasers with parallel polarization that should be considered in the future. This improvement because of polarization is however minor in comparison to the advantage of using the semi-forward scattering direction as can be seen by reduced $RMSE$ for these angles. This $RMSE$ affects the uncertainty of the calibration curve parameters a and b.

The center angle of the camera will also greatly affect the scattering intensity of the droplets and therefore also the range of sizes that are possible to measure. From the found smallest and largest size in the calibration, an extrapolation can be performed from the scattering theory. The smallest detectable size go from 1.7 to 14 µm and largest from around 22 to 245 µm when the center angles range from 30° to 100°. These sizes are valid for droplets that are stationary and in focus and the detection limit for moving droplets will follow the trends shown in Fig. 7(d) and (e). Note that lowering the center angle of the setup has not only a down side in a decrease of the maximum detection limit. The droplets are also moving relatively faster and are more densely packed in the camera projection. This increases the displacement-spacing ratio introduced in Section 5.1 that will lead to more tracking errors.

Finally the sizable range depending on the laser power is considered. The two lasers in this work contribute 4 W and 5 W independently that combined to 9 W continuous power. The scattering intensity can be assumed to be proportional to the laser power so one can approximate the new sizing limits from eq (1). When the power is changed the intensity is scaled with power P as $c = P/9$. That gives a scale of diameter c^b. The found min and max diameters for sizing with powers ranging from 1 to 12 W is shown in Fig. 10(c). Again, the size-range is valid for only stationary droplets. The possibility to size smaller droplets is the main reason for using the combined power of two lasers.

7. Conclusions

This work has introduced in detail an approach using high-speed scattered-light imaging for sizing of respiratory droplets. A continuous wave laser illuminates the droplets that scatter light into the camera placed in a semi-forward detection configuration. A second high-speed shadowgraph camera is used during calibration to find droplet size. Correspondences between droplet size and scattering intensity is used to extract a calibration curve. The calibrated setup is then applied on coughing respiratory events.

Following a detailed calibration procedure, the uncertainty of the sizing is found to be around 8% with a larger uncertainty of 12% for the smallest droplets. The limiting minimum and maximum sizes depend on the droplet speeds. A higher speed spread out the scattering intensity over multiple pixels during a single exposure and increases both the minimum and maximum detectable sizes. The size limits for stationary droplets are found from the calibration curve to be 3.4–44 μm. However, since the droplets seem to be generally faster than 5 m/s the sizing limits are increased to 4–80 μm.

The camera is placed in the semi-forward scattering direction (52°) that both improve the sizing accuracy according to the Lorenz–Mie theory and increase the scattering intensity. The increased intensity makes it possible to detect droplets as small as 3.4 μm in contrast to a perpendicular detection (90°) configuration that would be limited to around 10 μm. However, the increased scattering intensity also lowers the limit of largest possible droplet to size from 230 μm in the perpendicular direction to 44 in the semi-forward direction for stationary droplets.

It was concluded that a too thin illumination volume relative to the speed of the droplets and the imaging frame rate is not suitable for sizing by scattering intensity. The reason is that droplets cannot be guaranteed to be fully illuminated at any frame. The used 15 mm illumination thickness is wide enough to avoid this problem but because of this wide illumination, droplet tracking is required.

The droplet sizing was applied on respiratory droplets that were produced by subjects coughing. One cough from three different subjects were analyzed. The results show no clear change in average size spatially or temporally for a single cough. Generally more droplets are found in the spatial center of the cough jet.

In the future, a detailed analysis of the counting efficiency of this technique is required. In addition, analysis of how it compares to other sizing techniques using imaging will be of great use. Then, the sizing technique opens up new possibilities for understanding how droplets of different sizes are distributed both in space and time and how this varies between each unique respiratory event. In addition, the technique can be combined with stereoscopic imaging to extract both 3D velocities and size of the same droplets. When applied to different events of multiple subjects, the results can give valuable input information to modelers for analyzing complex situations involving airborne spreading of disease.

CRediT authorship contribution statement

Adrian Roth: Conceptualization, Methodology, Software, Validation, Formal analysis, Writing – original draft, Writing – review & editing, Visualization. **David Frantz:** Conceptualization, Methodology, Validation, Investigation, Writing – review & editing, Visualization. **Mehdi Stiti:** Conceptualization, Methodology, Validation, Investigation, Writing – review & editing, Visualization. **Edouard Berrocal:** Conceptualization, Methodology, Validation, Investigation, Writing – review & editing, Visualization, Supervision, Funding acquisition.

Declaration of competing interest

The authors declare that they have no known competing financial interests or personal relationships that could have appeared to influence the work reported in this paper.

Data availability

Data will be made available on request.

Acknowledgments

This work was supported by the European Research Council (Starting Grant 638546), the Crafoord Foundation, Sweden (20210942), the Swedish Research Council (2021-04542) and the Swedish Foundation for Strategic research (ITM17-0152).

Ethics statement

This work is a non-clinical study where no personal information except health status and sex was gathered and the study had no intent nor significant risk of affecting the subjects physically or mentally. This does not require an official ethical permission from the Swedish Ethical Review Authority. An informed consent and agreement from all participants involved in the measurements was signed.

Appendix A. Supplementary data

Supplementary material related to this article can be found online at https://doi.org/10.1016/j.jaerosci.2023.106257.

References

Adrian, R. J. (1984). Scattering particle characteristics and their effect on pulsed laser measurements of fluid flow: speckle velocimetry vs particle image velocimetry. *Applied Optics*, *23*(11), 1690–1691.

Alsved, M., Matamis, A., Bohlin, R., Richter, M., Bengtsson, P.-E., Fraenkel, C.-J., Medstrand, P., & Löndahl, J. (2020). Exhaled respiratory particles during singing and talking. *Aerosol Science and Technology*, *54*(11), 1245–1248. http://dx.doi.org/10.1080/02786826.2020.1812502.

Anfinrud, P., Stadnytskyi, V., Bax, C. E., & Bax, A. (2020). Visualizing speech-generated oral fluid droplets with laser light scattering. *New England Journal of Medicine*, *382*(21), 2061–2063. http://dx.doi.org/10.1056/NEJMc2007800.

Asadi, S., Wexler, A. S., Cappa, C. D., Barreda, S., Bouvier, N. M., & Ristenpart, W. D. (2019). Aerosol emission and superemission during human speech increase with voice loudness. *Scientific Reports*, *9*(1), 2348. http://dx.doi.org/10.1038/s41598-019-38808-z.

Bagheri, G., Schlenczek, O., Turco, L., Thiede, B., Stieger, K., Kosub, J. M., Clauberg, S., Pöhlker, M. L., Pöhlker, C., Moláček, J., Scheithauer, S., & Bodenschatz, E. (2023). Size, concentration, and origin of human exhaled particles and their dependence on human factors with implications on infection transmission. *Journal of Aerosol Science*, *168*, Article 106102. http://dx.doi.org/10.1016/j.jaerosci.2022.106102.

Bahl, P., de Silva, C., MacIntyre, C. R., Bhattacharjee, S., Chughtai, A. A., & Doolan, C. (2021). Flow dynamics of droplets expelled during sneezing. *Physics of Fluids*, *33*(11), http://dx.doi.org/10.1063/5.0067609.

Bar-On, Y. M., Flamholz, A., Phillips, R., & Milo, R. (2020). SARS-CoV-2 (COVID-19) by the numbers. In M. B. Eisen (Ed.), *eLife*, *9*, Article e57309. http://dx.doi.org/10.7554/eLife.57309.

Bertens, G., Bagheri, G., Xu, H., Bodenschatz, E., & Moláček, J. (2021). In situ cloud particle tracking experiment. *Review of Scientific Instruments*, *92*(12), Article 125105. http://dx.doi.org/10.1063/5.0065806.

Bohren, C. F., & Hoffman, D. R. (1983). Appendixes: Computer programs. In *Absorption and scattering of light by small particles* (pp. 475–476). John Wiley & Sons, Ltd, http://dx.doi.org/10.1002/9783527618156.app1.

Bourouiba, L. (2020). Turbulent gas clouds and respiratory pathogen emissions: Potential implications for reducing transmission of COVID-19. *JAMA*, http://dx.doi.org/10.1001/jama.2020.4756.

Bourouiba, L., Dehandschoewercker, E., & Bush, J. W. (2014). Violent expiratory events: on coughing and sneezing. *Journal of Fluid Mechanics*, *745*, 537–563.

Chao, C., Wan, M., Morawska, L., Johnson, G., Ristovski, Z., Hargreaves, M., Mengersen, K., Corbett, S., Li, Y., Xie, X., & Katoshevski, D. (2009). Characterization of expiration air jets and droplet size distributions immediately at the mouth opening. *Journal of Aerosol Science*, *40*(2), 122–133. http://dx.doi.org/10.1016/j.jaerosci.2008.10.003.

Clark, A., Machicoane, N., & Aliseda, A. (2019). A quantitative study of track initialization of the four-frame best estimate algorithm for three-dimensional Lagrangian particle tracking. *Measurement Science & Technology*, *30*(4), Article 045302. http://dx.doi.org/10.1088/1361-6501/ab0786.

de Silva, C. M., Bahl, P., Doolan, C., & Raina MacIntyre, C. (2021). Bespoke flow experiments to capture the dynamics of coughs and sneezes. *Measurement Science & Technology*, *32*(12), Article 125302. http://dx.doi.org/10.1088/1361-6501/ac2010.

Duguid, J. P. (1946). The size and the duration of air-carriage of respiratory droplets and droplet-nuclei. *Epidemiology & Infection*, *44*(6), 471–479. http://dx.doi.org/10.1017/S0022172400019288.

Fischer, E. P., Fischer, M. C., Grass, D., Henrion, I., Warren, W. S., & Westman, E. (2020). Low-cost measurement of face mask efficacy for filtering expelled droplets during speech. *Science Advances*, *6*(36), eabd3083. http://dx.doi.org/10.1126/sciadv.abd3083.

Goldman, E. (2020). Exaggerated risk of transmission of COVID-19 by fomites. *The Lancet Infectious Diseases*, *20*(8), 892–893. http://dx.doi.org/10.1016/S1473-3099(20)30561-2.

Gralton, J., Tovey, E., McLaws, M.-L., & Rawlinson, W. D. (2011). The role of particle size in aerosolised pathogen transmission: A review. *Journal of Infection*, *62*(1), 1–13. http://dx.doi.org/10.1016/j.jinf.2010.11.010.

Hamed, R., & Fiegel, J. (2014). Synthetic tracheal mucus with native rheological and surface tension properties. *Journal of Biomedical Materials Research Part A*, *102*(6), 1788–1798. http://dx.doi.org/10.1002/jbm.a.34851.

Han, H.-S., Sreenath, A., Birkeland, N. T., & Chancellor, G. J. (2011). Performance of a high resolution optical particle spectrometer. In *European aerosol conference, 2011*. Manchester, UK: URL https://tsi.com/getmedia/018aa941-ff26-4f57-877a-0cf051f1fcf7/Han_OPS_poster_for_EAC2011-8P291-A4?ext=.pdf.

Humphrey, S. P., & Williamson, R. T. (2001). A review of saliva: Normal composition, flow, and function. *The Journal of Prosthetic Dentistry*, *85*(2), 162–169. http://dx.doi.org/10.1067/mpr.2001.113778.

Johnson, G. R., Morawska, L., Ristovski, Z. D., Hargreaves, M., Mengersen, K., Chao, C. Y. H., Wan, M. P., Li, Y., Xie, X., Katoshevski, D., & Corbett, S. (2011). Modality of human expired aerosol size distributions. *Journal of Aerosol Science*, *42*(12), 839–851. http://dx.doi.org/10.1016/j.jaerosci.2011.07.009.

Katz, J., & Sheng, J. (2010). Applications of holography in fluid mechanics and particle dynamics. *Annual Review of Fluid Mechanics*, *42*(1), 531–555. http://dx.doi.org/10.1146/annurev-fluid-121108-145508.

Laven, P. (2003). Simulation of rainbows, coronas, and glories by use of Mie theory. *Applied Optics*, *42*(3), 436–444. http://dx.doi.org/10.1364/AO.42.000436.

Lebigot, E. O. (2020). Version: 3.1.5, Uncertainties: a Python package for calculations with uncertainties, URL http://pythonhosted.org/uncertainties/.

Lee, J., Yoo, D., Ryu, S., Ham, S., Lee, K., Yeo, M., Min, K., & Yoon, C. (2019). Quantity, size distribution, and characteristics of cough-generated aerosol produced by patients with an upper respiratory tract infection. *Aerosol and Air Quality Research*, *19*(4), 840–853. http://dx.doi.org/10.4209/aaqr.2018.01.0031.

Lewis, D. (2021). COVID-19 rarely spreads through surfaces. So why are we still deep cleaning? *Nature*, *590*(7844), 26–28. http://dx.doi.org/10.1038/d41586-021-00251-4.

Li, Y. (2021). Basic routes of transmission of respiratory pathogens—A new proposal for transmission categorization based on respiratory spray, inhalation, and touch. *Indoor Air*, *31*(1), 3–6. http://dx.doi.org/10.1111/ina.12786.

Lindsley, W. G., Pearce, T. A., Hudnall, J. B., Davis, K. A., Davis, S. M., Fisher, M. A., Khakoo, R., Palmer, J. E., Clark, K. E., Celik, I., Coffey, C. C., Blachere, F. M., & Beezhold, D. H. (2012). Quantity and size distribution of cough-generated aerosol particles produced by influenza patients during and after illness. *Journal of Occupational and Environmental Hygiene*, *9*(7), 443–449. http://dx.doi.org/10.1080/15459624.2012.684582.

Liu, Y., Ning, Z., Chen, Y., Guo, M., Liu, Y., Gali, N. K., Sun, L., Duan, Y., Cai, J., Westerdahl, D., Liu, X., Xu, K., Ho, K.-f., Kan, H., Fu, Q., & Lan, K. (2020). Aerodynamic analysis of SARS-CoV-2 in two Wuhan hospitals. *Nature*, *582*(7813), 557–560. http://dx.doi.org/10.1038/s41586-020-2271-3.

Mahjoub Mohammed Merghani, K., Sagot, B., Gehin, E., Da, G., & Motzkus, C. (2021). A review on the applied techniques of exhaled airflow and droplets characterization. *Indoor Air*, *31*(1), 7–25. http://dx.doi.org/10.1111/ina.12770.

Misawa, T., & Yonamoto, Y. (2021). Imaging-based particle sizing system combining scattered-light imaging and particle-shade imaging for submicron particles. *Powder Technology*, *394*, 1218–1230. http://dx.doi.org/10.1016/j.powtec.2021.09.011.

Morawska, L., Allen, J., Bahnfleth, W., Bluyssen, P. M., Boerstra, A., Buonanno, G., Cao, J., Dancer, S. J., Floto, A., Franchimon, F., Greenhalgh, T., Haworth, C., Hogeling, J., Isaxon, C., Jimenez, J. L., Kurnitski, J., Li, Y., Loomans, M., Marks, G., ... Yao, M. (2021). A paradigm shift to combat indoor respiratory infection. *Science*, *372*(6543), 689–691. http://dx.doi.org/10.1126/science.abg2025.

Morawska, L., Johnson, G., Ristovski, Z., Hargreaves, M., Mengersen, K., Corbett, S., Chao, C., Li, Y., & Katoshevski, D. (2009). Size distribution and sites of origin of droplets expelled from the human respiratory tract during expiratory activities. *Journal of Aerosol Science*, *40*(3), 256–269. http://dx.doi.org/10.1016/j.jaerosci.2008.11.002.

Ouellette, N. T., Xu, H., & Bodenschatz, E. (2006). A quantitative study of three-dimensional Lagrangian particle tracking algorithms. *Experiments in Fluids*, *40*(2), 301–313. http://dx.doi.org/10.1007/s00348-005-0068-7.

Papineni, R. S., & Rosenthal, F. S. (1997). The size distribution of droplets in the exhaled breath of healthy human subjects. *Journal of Aerosol Medicine*, *10*(2), 105–116. http://dx.doi.org/10.1089/jam.1997.10.105.

Ragucci, R., Cavaliere, A., & Massoli, P. (1990). Drop sizing by laser light scattring exploiting intensity angular oscillation in the mie regime. *Particle & Particle Systems Characterization*, *7*(1–4), 221–225. http://dx.doi.org/10.1002/ppsc.19900070136.

Roth, A., Stiti, M., Frantz, D., & Berrocal, E. (2022). Stereoscopic high-speed imaging for 3D tracking of coughed saliva droplets in the context of COVID-19 spreading. In *20th international symposium on applications of laser and imaging techniques to fluid mechanics, 2022*. Lisbon, Portugal: URL https://portal.research.lu.se/en/publications/stereoscopic-high-speed-imaging-for-3d-tracking-of-coughed-saliva.

Russell, P. S., Barbaca, L., Venning, J. A., Pearce, B. W., & Brandner, P. A. (2020). Measurement of nuclei seeding in hydrodynamic test facilities. *Experiments in Fluids*, *61*(3), 79. http://dx.doi.org/10.1007/s00348-020-2911-2.

Shao, S., Zhou, D., He, R., Li, J., Zou, S., Mallery, K., Kumar, S., Yang, S., & Hong, J. (2021). Risk assessment of airborne transmission of COVID-19 by asymptomatic individuals under different practical settings. *Journal of Aerosol Science*, *151*, Article 105661. http://dx.doi.org/10.1016/j.jaerosci.2020.105661.

Sjoeberg, H., Manneberg, G., & Cronhjort, A. (1996). Long-working-distance microscope used for diesel injection spray imaging. *Optimization and Engineering*, *35*(12), 3591–3596. http://dx.doi.org/10.1117/1.601113.

Stiti, M., Castanet, G., Corber, A., Alden, M., & Berrocal, E. (2022). Transition from saliva droplets to solid aerosols in the context of COVID-19 spreading. *Environmental Research*, *204*, Article 112072. http://dx.doi.org/10.1016/j.envres.2021.112072.

van de Hulst, H. C. (1957). *Light scattering by small particles*. Wiley.

Wang, C. C., Prather, K. A., Sznitman, J., Jimenez, J. L., Lakdawala, S. S., Tufekci, Z., & Marr, L. C. (2021). Airborne transmission of respiratory viruses. *Science*, *373*(6558), eabd9149. http://dx.doi.org/10.1126/science.abd9149.

Webber, B. F., Long, M. B., & Chang, R. K. (1979). Two-dimensional average concentration measurements in a jet flow by Raman scattering. *Applied Physics Letters*, *35*(2), 119–121. http://dx.doi.org/10.1063/1.91042.

WHO (2014). Infection prevention and control of epidemic-and pandemic prone acute respiratory infections in health care. URL https://www.who.int/publications-detail-redirect/infection-prevention-and-control-of-epidemic-and-pandemic-prone-acute-respiratory-infections-in-health-care.

Xie, X., Li, Y., Sun, H., & Liu, L. (2009). Exhaled droplets due to talking and coughing. *Journal of the Royal Society Interface*, *6*(suppl_6), S703–S714. http://dx.doi.org/10.1098/rsif.2009.0388.focus.

Yang, S., Lee, G. W., Chen, C.-M., Wu, C.-C., & Yu, K.-P. (2007). The size and concentration of droplets generated by coughing in human subjects. *Journal of Aerosol Medicine*, *20*(4), 484–494. http://dx.doi.org/10.1089/jam.2007.0610.